Radiation damage and defect dynamics in 2D WS2

de Graaf, Sytze; Kooi, Bart J.

Published in:
2D Materials

DOI:
10.1088/2053-1583/ac3377

Radiation damage and defect dynamics in 2D WS_2: a low-voltage scanning transmission electron microscopy study

IOP Publishing 2D Mater. 9 (2022) 015009 https://doi.org/10.1088/2053-1583/ac3377

2D Materials

PAPER

Radiation damage and defect dynamics in 2D WS_2: a low-voltage scanning transmission electron microscopy study

Sytze de Graaf and Bart J Kooi

Zernike Institute for Advanced Materials, University of Groningen, 9747 AG Groningen, The Netherlands

E-mail: sytze.de.graaf@rug.nl **and** b.j.kooi@rug.nl

Keywords: 2D materials, transition metal dichalcogenides, electron radiation damage, defect dynamics, low-voltage scanning transmission electron microscopy, integrated differential phase contrast, electrostatic potential imaging

Supplementary material for this article is available online

OPEN ACCESS

RECEIVED
21 July 2021

REVISED
4 October 2021

ACCEPTED FOR PUBLICATION
26 October 2021

PUBLISHED
12 November 2021

Abstract

Modern low-voltage scanning transmission electron microscopes (STEMs) have been invaluable for the atomic scale characterization of two-dimensional (2D) materials. Nevertheless, the observation of intrinsic structures of semiconducting and insulating 2D materials with 60 kV-microscopes has remained problematic due to electron radiation damage. In recent years, ultralow-voltage microscopes have been developed with the prospects of minimizing radiation damage of such 2D materials, however, to date only ultralow-voltage TEM investigations of semiconducting and insulating 2D materials have been reported, but similar results using STEM, despite being more widely adopted, are still missing. Here we report a quantitative analysis of radiation damage and beam-induced defect dynamics in semiconducting 2D WS_2 during 30 kV and 60 kV-STEM imaging, particularly by recording atomic resolution electrostatic potential movies using integrated differential phase contrast to visualize both the light sulfur and heavy tungsten atoms. Our results demonstrate that electron radiation damage of 2D WS_2 aggravates by a factor of two when halving the electron beam energy from 60 keV to 30 keV, from which we conclude electronic excitation and ionization to be the dominant mechanism inducing defects and damage during low-voltage STEM imaging of semiconducting 2D materials.

1. Introduction

Two-dimensional transition metal dichalcogenides (2D TMDs) host a variety of unique properties, unavailable in their bulk counterparts, that are attractive for fundamental condensed-matter research and applications including (opto) electronics, photonics [1, 2], spintronics [3] and sensing [4]. The tunable properties are the virtue of TMDs, enabled by their strong structure-property relationship via the diverse chemical compositions, various crystal phases and rich library of defects [5].

Aberration-corrected (scanning) transmission electron microscopy (TEM) has been most valuable for the characterization of 2D TMDs. Specifically scanning TEM (STEM) is the best available tool for atomic resolution imaging and chemical characterization, and also for the manipulation down to the level of single atoms [6, 7]. Damage free imaging of conductive 2D materials like graphene has been facilitated by modern low-voltage microscopes that operate below the knock-on damage threshold, which is typically 80 kV [8]. Then the primary electrons cannot transfer sufficient energy to displace or sputter single atoms upon a head-on elastic collision with the atom nuclei. At the same time, insulating and semiconducting 2D materials like many TMDs, suffer from electronic excitation and ionization damage by inelastic scattering of the primary energetic electron by the atom's electron cloud, which starts dominating when the electron beam energy decreases below the knock-on threshold. In addition, 2D materials can also be damaged by chemical etching with oxygen radicals that are formed by the electron beam from the residual gases in the microscope column and water on the specimen, which can be minimized by an (ultra) high-vacuum environment and clean specimens [9]. Due to the balance of knock-on

displacement damage and ionization damage, it is expected that electron radiation damage can never be fully prevented for insulating or semiconducting 2D materials [10–12].

Nevertheless, with the ultimate goal to image intrinsic structures of 2D materials with STEM, it is extremely valuable to know which electron beam energy is most suitable for the imaging of semiconducting 2D materials while minimizing radiation damage. To date, however, it is not well understood which damage mechanisms are at play in 2D materials at (ultra) low-voltages, despite the development of state-of-the-art ultralow-voltage microscopes operating at 30 kV [13], 20 kV [14, 15] and 15 kV [16]. Interestingly, all quantitative investigations of radiation damage are TEM based, but similar results for the principally different STEM are missing, despite being widely adopted by the 2D materials science community.

Here we report quantitative radiation damage analysis and electron beam-induced creation and evolution of defects in the semiconducting 2D TMD WS_2, by recording atomic resolution movies using 30 kV and 60 kV-STEM. To visualize the light sulfur and heavier tungsten atoms simultaneously, we employ electrostatic potential imaging with integrated differential phase contrast (iDPC)-STEM [17], next to the common annular dark-field (ADF)-STEM, which is more sensitive to heavy elements. It has recently been demonstrated that 30 kV iDPC-STEM is capable of imaging single sulfur atoms and its dynamics in 2D WS_2, which are often practically invisible in ADF-STEM images [18]. In general, iDPC-STEM is the most robust method to image light elements next to heavy ones in various materials systems, including the imaging of oxygen atoms in hafnia-based ferroelectric devices [19, 20], single molecules in the channels of zeolites [21], and hydrogen atoms in titanium hydride [22]. Importantly, iDPC-STEM is currently the only option for the direct and fast acquisition of atomic electrostatic potential movies, as it has a major speed advantage over the competing integrated center of mass (iCOM)-STEM [23] and electron ptychography [24], which are practically limited to single images due to its orders of magnitude slower pixelated detectors, large datasets and extensive postprocessing.

2. Experimental methods

2D WS_2 flakes were transferred from a silicon wafer to a Quantifoil TEM grid using a clean polymer free method as described previously [18]. A double aberration corrected 30–300 kV Thermo Fisher Scientific Themis Z S/TEM operating at 30 kV and 60 kV was used for the acquisition of atomic resolution movies of 2D WS_2, with minimal geometrical and chromatic aberrations employing the S-CORR probe corrector and electron monochromator, respectively. For the 30 kV-STEM imaging the probe convergence semi-angle was 33 mrad, the probe current 2.5–7.5 pA (depending on energy selecting aperture size), probe step size 15.9–22.5 pm, and the dwell time 40–50 μs. The collection angles of the segmented DF4 detector (for iDPC-STEM imaging) and ADF detector were 9–36 mrad and 39–200 mrad, respectively. For the 60 kV-STEM imaging the probe convergence semi-angle was 28 mrad, the probe current 15 pA, probe step size 23.52 pm, and the dwell time 10 μs. The collection angles of the segmented DF4 detector (for iDPC-STEM imaging) and ADF detector were 7–29 mrad and 31–186 mrad, respectively. The movies are processed with Fiji [25, 26] using the 'FFT Bandpass Filter', with a low-pass filter of 3 pixels, and high-pass filter of 10 pixels, a standard operation in 2D materials research to optimize image quality.

3. Results and discussion

In figure 1 we show atomic resolution images of simple defects in 2D WS_2 that are induced by the 30 keV and 60 keV electron beam. Images of a sulfur vacancy (V_S) and a sulfur divacancy (V_{S2}) are shown in figures 1(a) and (b) (30 kV) and figures 1(e) and (f) (60 kV). Note that the images are extracted from movies for studying the defect dynamics and are thus not optimized high-dose single shot images (see movie S1 (available online at stacks.iop.org/2DM/9/015009/mmedia) for 30 kV-STEM and movie S2 for 60 kV-STEM).

Despite the lower dose imaging conditions, the V_S and V_{S2} defects are still identifiable and also differentiable in iDPC-STEM images for both accelerating voltages, as opposed to the ADF-STEM images. In the latter case the low signal from sulfur atoms combined with the lack of contrast between one and two sulfur atoms, complicates the robust identification of V_S and V_{S2}. Other commonly reported defects that we also observe are mirror grain boundaries (figures 1(g)–(i)) and sulfur vacancy lines (figures 1(j)–(l)). The mirror twin grain boundaries are observed in the 4|4P form (according to the notation of [27]) with four-fold rings sharing a common chalcogen column (figures 1(g)–(i)), and also in the 4|4E form which has a structure similar to a double sulfur vacancy line. The mirror twin boundaries and sulfur vacancy lines generally form a connected network after prolonged exposure, which leads to inversion domains when forming a closed loop (see figure S1) [28]. The sulfur vacancy lines generally do not exceed a width of two sulfur atoms but occasionally grow wider similar to [29]. Hence, the sulfur atoms are also more clearly resolved in iDPC-STEM images of such line defects. Thus, electrostatic potential imaging with iDPC-STEM enables a more complete atom-by-atom evaluation of defect structures than ADF-STEM, even

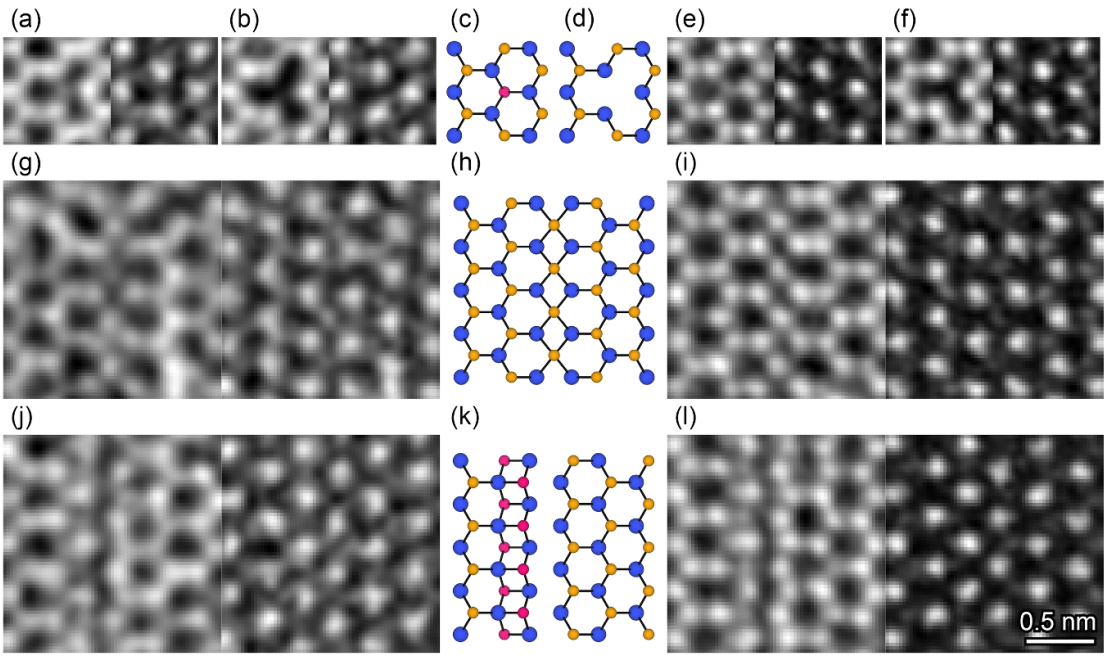

Figure 1. Atomic resolution images of common beam-induced defects in 2D WS_2. Thirty kilovolt iDPC-STEM (left panels) and ADF-STEM (right panels) images, respectively, of a (a) sulfur vacancy, (b) sulfur divacancy, (g) mirror twin grain boundary, (j) sulfur vacancy line. And similarly, 60 kV iDPC-STEM (left panels) and ADF-STEM (right panels) images of a (e) sulfur vacancy, (f) sulfur divacancy, (i) mirror twin grain boundary, (l) sulfur vacancy line. The generic idealized schematic models of a sulfur vacancy, sulfur divacancy, mirror twin boundary and double sulfur vacancy line are shown in (c), (d), (h) and (k), respectively. In the models W, S_2 and S are blue, orange and pink, respectively. Scale bar in (l) applies to all panels.

in cases of low-dose imaging. Such detailed experimental information on the beam-induced evolution of atomic structure is valuable for advancing the understanding of electron–matter interactions which in the end can contribute to the development of damage free imaging of matter with electron microscopes.

In an effort to investigate which electron–matter interactions are active during the low-voltage STEM imaging, we quantify the complete creation and evolution of defects in the atomic resolution movies, by measuring frame-by-frame the density of point defects, line defects and holes. To this end the single sulfur atom sensitivity of electrostatic potential imaging using iDPC-STEM is crucial, because the relatively light sulfur atoms have reduced intensity in ADF-STEM images, making their robust detection more challenging, in fact, often impossible. Using a template matching approach we have extracted the sulfur vacancy density for every frame in the movie as shown in figures 2(a) and (b). The next stage of beam-induced damage is the rapid nucleation and growth of sulfur vacancy lines. The contracted W–W distance perpendicular to the line defects relative to the pristine W sublattice allows identification of such defects with a strain analysis method. We employ a real-space strain analysis approach, which we found to be more robust than a reciprocal space method like geometrical phase analysis (figure 2(c)). Briefly, first the atom coordinates of the W atoms are detected in the ADF-STEM images with a scale-space method, then the W–W nearest-neighbor distance relative to the mean W–W distance is calculated and are averaged for every atom (see supplementary material (SM) for detailed information). For this purpose the ADF-STEM images have an advantage over iDPC-STEM images, because the W and S_2 sublattices are readily separated by intensity thresholding in ADF-STEM images. This is not the case in in the iDPC-STEM images where the W and S_2 intensities are very similar.

Finally, holes appear after prolonged exposure to the electron beam, which we identify based on intensity thresholding combined with the criterium of a minimal area slightly larger than point defects (figure 2(d)). In general the holes appear at highly defective regions, e.g. at the intersection of line defects, or agglomerates of point defects, and are therefore also correlated with the material's defect history [29–31].

The resulting quantitative analysis of all defect stages is plotted in figures 2(e) and (f) as a function of electron dose, which is defined in detail in the SM section 2. We have fitted the evolution of sulfur vacancies and the growth of holes as a function of electron dose with an asymptotic exponential function, and the growth of line defects with a linear function. The physical interpretation of the exponential function is that the generation rate of sulfur

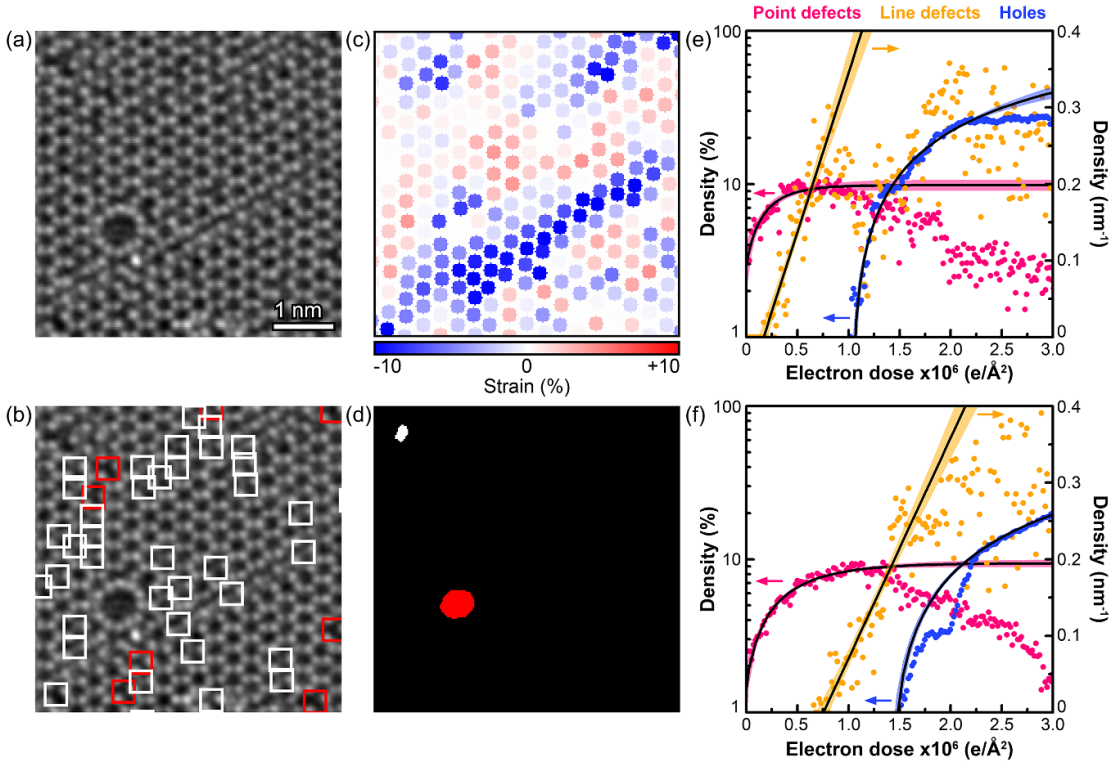

Figure 2. Quantitative analysis of electron radiation damage in 2D WS_2 during low-voltage 30 kV and 60 kV STEM imaging. (a) Single frame containing point defects, line defects and a hole, selected from a 60 kV iDPC-STEM movie. (b) Sulfur vacancies (white squares) and divacancies (red squares) are detected with template matching. (c) Line defect are identified as areas of compressive stress (blue points) based on real-space strain analysis. (d) Holes are found by intensity thresholding, of which only those larger than point defects (red area) are selected and smaller ones are ignored (white area). Quantitative evolution of the three stages of radiation damage including fitting with 95% confidence band is plotted in (e) for 30 kV-STEM and (f) for 60 kV-STEM.

vacancies and growth rate of holes is proportional to the accumulated electron dose and the remaining sulfur atoms and material, respectively. The trend of sulfur vacancy densities evolution is similar for both accelerating voltages: it increases according to the asymptotic exponential function and saturates close to 10%, after which it gradually decays.

The indirect measurement of the sulfur vacancy line density renders it rather noisy, and is not reliable once the crystal is substantially damaged and other areas with contracted W–W distances are formed. Nevertheless, sulfur vacancy line density measurement is reliable in the initial stage including nucleation and growth. They appear once the sulfur vacancy density exceeds 6%–8%, and, to a first approximation, grow about linearly in length with the accumulated electron dose. Moreover, the nucleation of the sulfur vacancy lines appears to depend predominantly on the sulfur vacancy density and not on the electron beam energy, in agreement with the consensus in literature that sulfur vacancy lines are sinks of sulfur vacancies [30, 31].

An interesting observation is that the sulfur vacancy density (corrected for remaining area) decreases once small holes are formed. This suggests that there is a driving force for sulfur vacancies to migrate towards exposed edges during electron beam exposure. In other words, during the destruction of edges by the electron beam, sulfur atoms are not only sputtered into the vacuum, but some also migrate away and annihilate existing vacancies, rendering the holes as sulfur atom sources. This agrees with the typical formation of metallic tungsten clusters near holes that are deficient in sulfur atoms.

Comparing the overall progression of radiation damage as a function of total accumulated electron dose indicates that the radiation damage is aggravated when the electron beam energy is reduced from 60 keV to 30 keV (figures 2(e) and (f)). For quantification we computed the damage onsets and growth rates in terms of characteristic electron doses (reciprocal of the damage cross-section) based on the fitting parameters, which are summarized in table 1 (see SM section 2 for fitting methods).

Overall, the quantitative analysis demonstrates that the three main stages of radiation damage, point defects, line defects and holes, develop faster when the electron beam energy is 30 keV compared to 60 keV. The point defects and holes develop about twice as fast, and the line defects 1.4 times as fast with accumulated electron dose. The linearized cross-sections for sulfur vacancy formation during 30 kV and 60 kV STEM imaging are 3.96 ± 0.90 barn and 2.03 ± 0.21 barn, respectively, which are both about

Table 1. Fitted electron doses with corresponding standard deviation required for the initiation (onset dose) and growth (characteristic dose) of the three main stages in the radiation damage of 2D WS_2. Note that the sulfur vacancies density is defined as their total length per unit area in nanometer units.

	30 keV	60 keV	Factor
Sulfur vacancies characteristic dose (10^6 e Å^{-2})	0.25 ± 0.06	0.49 ± 0.05	2.0 ± 0.5
Sulfur vacancy lines onset dose (10^6 e Å^{-2})	0.17 ± 0.03	0.75 ± 0.08	4.5 ± 1.0
Sulfur vacancy lines characteristic dose (10^6 e Å^{-2})	2.4 ± 0.2	3.5 ± 0.2	1.4 ± 0.1
Holes onset dose (10^6 e Å^{-2})	1.03 ± 0.01	1.41 ± 0.01	1.37 ± 0.02
Holes characteristic dose (10^6 e Å^{-2})	3.9 ± 2	7.3 ± 0.7	1.9 ± 0.8

a factor two lower than those reported for similar TEM measurements on 2D MoS_2 [15]. The stochastic nature of the nucleation of these damage stages is reflected in the more random values for the onset (see also figure S2(a)). The nearly factor of two increase of radiation damage cross-section when decreasing the primary electron energy from 60 keV to 30 keV is in good agreement with the inelastic scattering cross-section (scaling as $1/E$) according to the Bethe theory [32, 33], which describes that more momentum and energy is transferred from the primary electrons to the atomic electrons as the velocity (v) of the incoming electrons decreases, resulting in a cross-section proportional to $1/v^2$, or equivalently $1/E$, for ionization [11]. Hence these results suggest that ionization is the dominant damage mechanism during the low-voltage STEM imaging of 2D WS_2, rather than elastic scattering effects like knock-on displacement or sputtering.

Moreover, we observe that the radiation damage during 30 kV-STEM imaging does not depend significantly on the time between consecutive electrons when it is varied from 4 ns to 64 ns (figure S2(b)). This suggests that there is not a significant dose rate effect in this range, implying the total accumulated electron dose to be the dominant parameter i.e. a high probe current with short dwell time, or low probe current with long dwell time, produces the same damage as long as the total electron dose is equivalent.

Next we focus on more exotic defects, that we observe during the recording of atomic resolution movies using 30 kV and also 60 kV-STEM using simultaneously iDPC-STEM and ADF-STEM for the unambiguous identification of all sulfur and tungsten atoms. To the best of our knowledge these defects have not been imaged before at 30 kV and also not using simultaneously iDPC-STEM and ADF-STEM at 60 kV. The first defect that we describe has been coined a trefoil defect, due to its peculiar three-fold symmetric shape that is the result of an effective 60° bond-rotation of the central six metal-chalcogen bonds [34, 35]. Interestingly, this defect has not been observed before in WS_2 at room temperature, but rather in its selenide counterpart.

With the electron beam energy of 60 keV we have never observed complete trefoil defects, only four partial trefoil defects in 400 frames. These partial defects consist of two eight-membered rings instead of three, and are always found directly next to existing sulfur vacancy lines. In figures 3(a)–(d) we show with iDPC-STEM images how such a defect structure appears near a sulfur vacancy line defect, and disappears two frames later. The simultaneously acquired ADF-STEM images are shown in figures 3(i)–(l), and are particularly useful to identify the W sublattice. The full dataset then readily allows the identification of all atoms from which the schematic in figures 3(e)–(h) is constructed.

In the first frame (figure 3(a)), several of the central tungsten atoms are substantially undercoordinated due to the two neighboring sulfur divacancies. These tungsten atoms are bonded to only two to four sulfur atoms instead of six, as schematically illustrated in figure 3(e). In the next frame (figure 3(b)), two sulfur atoms fill the void in the center of the divacancy cluster, forming two eight-membered rings and the effective 60° bond rotation. The single sulfur atom that was residing next to the divacancy cluster in the previous frame, has most likely moved to this position, considering that it requires the smallest possible displacement and its former position has now become vacant [34]. Hence, it is reasonable to infer that undercoordination of the tungsten atoms is the driving force for such effective bond rotations in partial trefoil defects. Next to the two eight-membered rings, at the position where the third ring would be present for a complete trefoil defect, five single sulfur atoms are visible in the iDPC-STEM image in figures 3(b) and (c), which can be interpreted as a local transformation from trigonal prismatic coordination to partial octahedral (as in the metallic 1 T structure) or tetrahedral coordination. A small lateral displacement of several S_2 columns is visible in the iDPC-STEM image as a blurred asymmetric peak on the right hand side next to the sulfur vacancy line (figure 3(b)). The overall trefoil structure remains stable for two frames (figures 3(b) and (c)), and then reverts back to the original lattice only including a cluster of five sulfur vacancies (figures 3(d) and (h)).

When the electron beam energy is 30 keV, the trefoil defects are about equally rare. In 200 frames we have observed one partial trefoil and also one complete trefoil, the latter is shown in figure 4. In this case the trefoil defect is fully three-fold symmetric and does not form next to line defects, as opposed

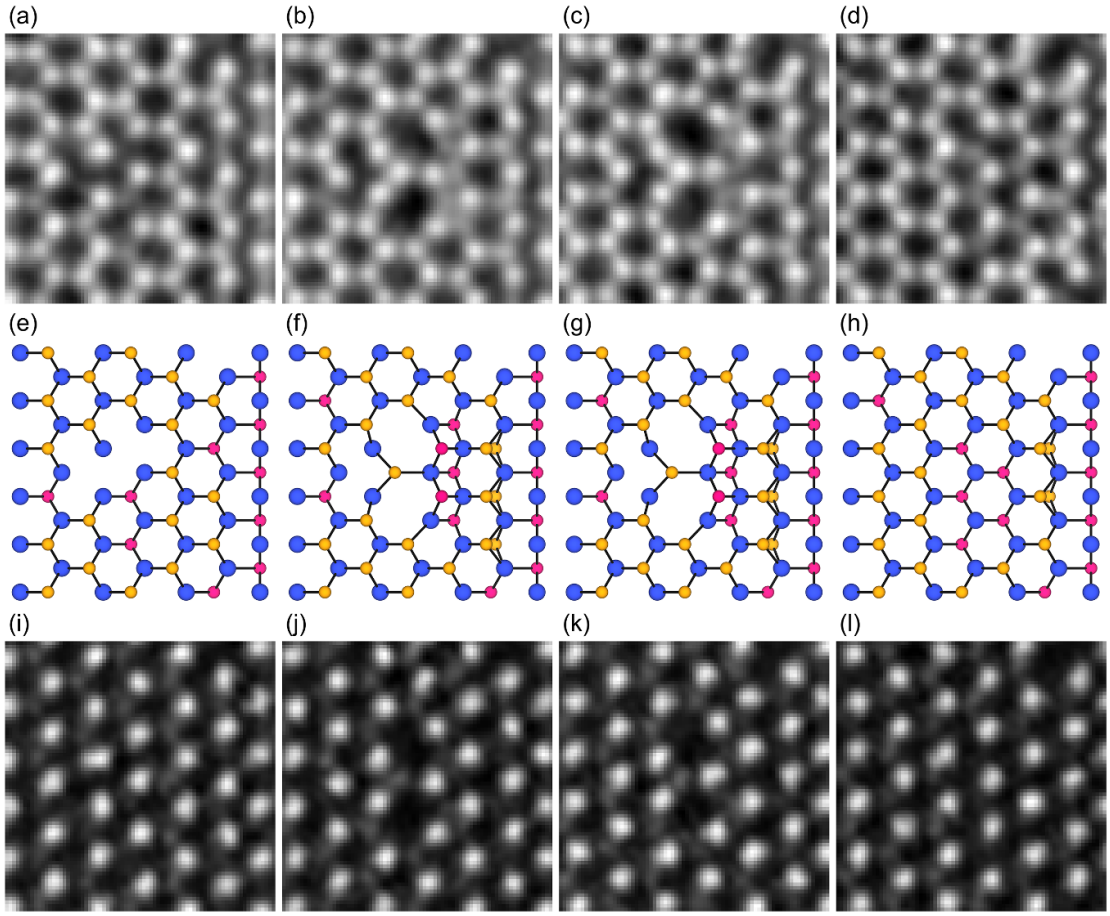

Figure 3. Electron beam-induced creation and healing of a partial trefoil defect next to a sulfur vacancy line during 60 kV-STEM imaging. (a)–(d) iDPC-STEM images. (e)–(h) Schematic structure evolution of the defect, with blue W atoms, orange S_2 columns, and pink single sulfur atoms (equivalent to sulfur vacancies). (i)–(l) Simultaneously acquired ADF-STEM images.

to the partial trefoil defects during 60 kV-STEM imaging. Also here we observe two sulfur divacancies (figure 4(a)), next to several sulfur vacancies, and relative displacements of sulfur atoms which we infer from the blurring of a sulfur column. In the next frame (figure 4(b)), the trefoil defect is present and has consumed several sulfur vacancies. The defect disappears already in the next frame as shown in figure 4(c).

The rare experimental observations of short lived trefoil defects during 30 kV and 60 kV-STEM imaging indicate that their formation is a rather stochastic process and thermodynamically unstable. This is agreement with first-principle calculations, that predict the trefoil defect to be unstable in WS_2 due to an 0.22 eV energy increase required for the bond rotation, which additionally has a substantial activation energy of 5.35 eV. This is opposite to the case of WSe_2, where the trefoil defect is stabilized by 1.31 eV and furthermore also has a reduced energy barrier of 3.12 eV, explaining why they are readily formed at room temperature [35]. The partial trefoil defect in WS_2 is also predicted to be unstable with a positive formation energy of 0.14 eV relative to a cluster of two sulfur divacancies [36]. Furthermore, the prerequisite for the formation of a trefoil defect is the clustering of chalcogen divacancies, requiring sufficiently mobile sulfur vacancies. Indeed, this clustering is a kinetically controlled stochastic process [34]. For this reason, trefoil defects have only been observed in WS_2 at elevated temperatures of 500 °C where the sulfur vacancy mobility is high [34, 37]. First-principle calculations predict the activation energy for sulfur vacancy migration in WS_2 to be at least 2.8–2.9 eV (and up to 4.6 eV when the lattice cannot relax sufficiently fast [35]) when no other vacancies are present nearby [35, 36]. However, this energy is expected (based on calculations for WSe_2 [35]) to decrease approximately linearly by as much as 80% (to 0.5–0.9 eV), when the number of sulfur vacancies in the direct vicinity increases to a maximum of six.

Sulfur vacancy lines may provide thermodynamic stabilization facilitating heterogeneous nucleation of partial trefoil defects, if this is the case the stabilization is expected to be minor considering that the partial trefoil defects are present for only several frames before they dissolve during 60 kV-STEM imaging. Alternatively, the sulfur vacancy lines may be a source and sink of sulfur

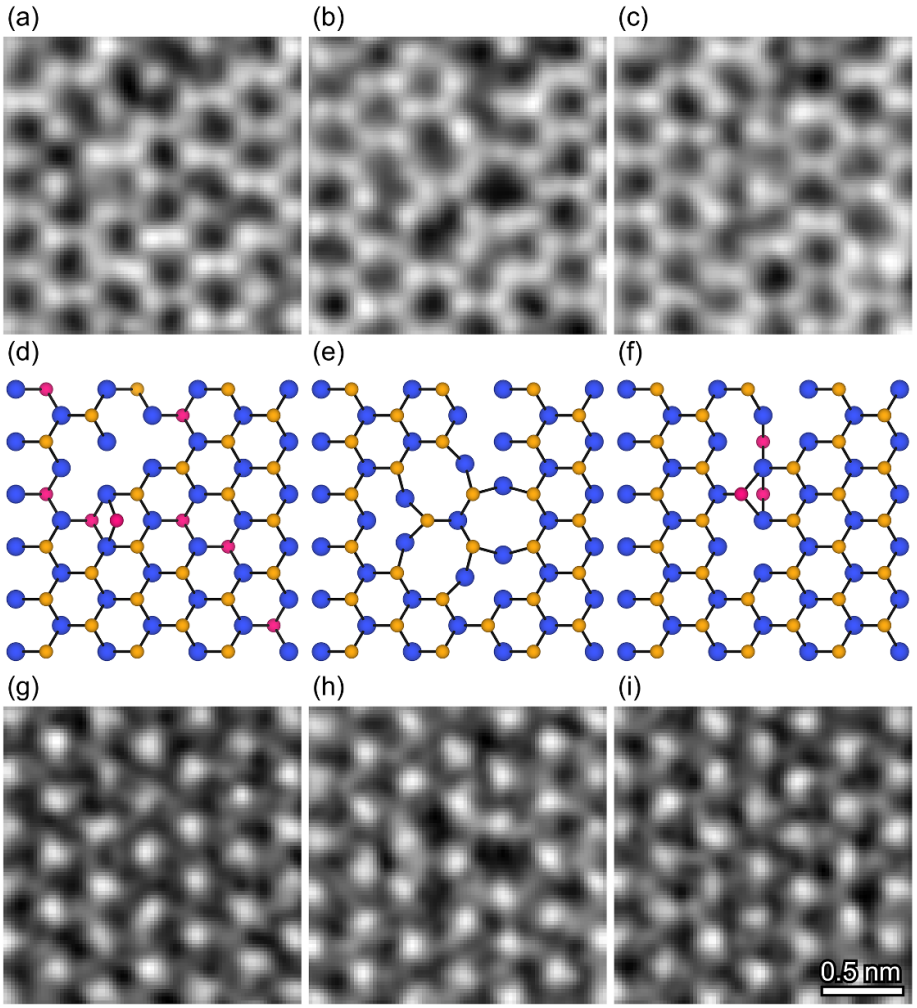

Figure 4. Electron beam-induced creation and healing of a complete trefoil defect during 30 kV-STEM imaging. (a)–(c) iDPC-STEM images. (d)–(f) Schematic structure evolution of the defect, with blue W atoms, orange S_2 columns, and pink single sulfur atoms (equivalent to sulfur vacancies). (g)–(i) Simultaneously acquired ADF-STEM images.

atoms due to the enhanced migration rate of atoms along these line defects enabled by lower binding energies [30], kinetically enhancing the nucleation rate of partial trefoil defects near sulfur vacancy lines.

The electron–matter interactions that provide energy for the formation of trefoil defects are a complex combination of elastic and inelastic scattering events [10, 15]. On the one hand, sulfur atom migration is possible (in particular when the sulfur vacancy density is high) by elastic scattering of the primary electrons from sulfur nuclei, even when the electron beam energy is 30 keV, because upon a head-on elastic collision of the primary electrons with the sulfur or tungsten nuclei, the maximum energy transfer is respectively, 4.35 eV and 0.76 eV (60 keV beam) and 2.11 eV and 0.37 eV (30 keV beam) [38]. On the other hand, the maximum energy transfer by elastic scattering is well below the high energy barriers that are involved in the formation of trefoil defects, particularly in case of the 30 keV electron beam. Therefore, predominantly inelastic scattering of the primary electrons from the atom's electron cloud causing electronic excitations must be involved in the formation of (partial) trefoil defects, in agreement with our quantitative radiation damage analysis.

The second defect that we describe here has a similar nature as the trefoil defect: a tungsten adatom induced bond rotational defect, which we observe during 30 kV and 60 kV-STEM imaging generally near sulfur vacancy lines or near the edges of holes. To the best of our knowledge, this defect type has not yet been reported.

In figure 5 we display the creation and evolution of this defect during 60 kV-STEM imaging. The adatom and the induced defect appear within one frame and generate a distinct triangular shape, particularly visible in the iDPC-STEM image (figure 5(b)), and is very stable until the WS_2 is fully destructed by the electron beam. We identify the adatom to be a W atom residing on top of another W atom in the WS_2 lattice, based on the twice as high intensity of this column in the ADF-STEM image (compare

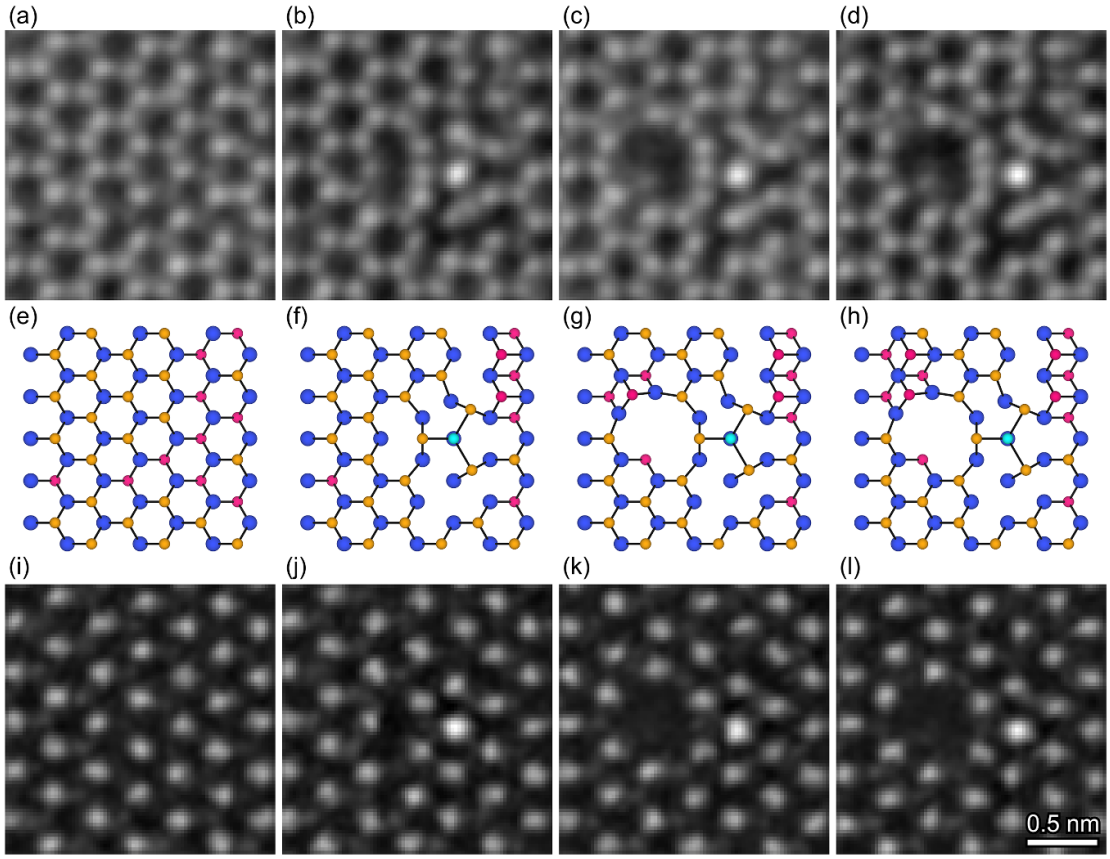

Figure 5. Creation and evolution of a W-adatom induced bond rotational defect and a sub-nanometer pore during 60 kV-STEM imaging. (a)–(d) iDPC-STEM images. (e)–(h) Schematic structure evolution of the defect, with blue W atoms, orange S_2 columns, pink single sulfur atoms and a cyan W adatom. (i)–(l) Simultaneously acquired ADF-STEM images.

figure 5(i) with figure 5(j)). The iDPC-STEM images in figures 5(a) and (b) clearly reveal that the central W–W column has attracted the next-nearest S atoms as their position has become vacant, at the same time, the nearest S atoms have either combined with the next-nearest S atoms or have been removed by the electron beam. This collective displacement mechanism leads to the effective 60° bond rotation with the central W–W column bonded to three S_2 columns, creating the triangular shape with straight W–S_2–W edges.

The formation of nanopores [37] next to the adatom defect is a typical secondary effect that occurs once one of the undercoordinated W atoms surrounding the adatom defect is removed by the electron beam, followed by the outward relaxation of the remaining undercoordinated S atoms that were previously bonded to the removed W atom (figure 5(c)) [37]. Such a relaxed edge structure (top left of the pore in figure 5(c)) likely passivates the undercoordinated S atom by forming again three stable S–W bonds, as schematically indicated in figure 5(g), similar to the case of the partial trefoil defect in figure 3(c). However, this edge structure is not always formed, as a single S atom remains protruding in the lower left part of the pore (figures 5(c) and (d)). In fact, the most stable edge structure contains not three single S atoms but rather one S_2 column as shown in figure S3, requiring the removal of several more S atoms.

A practically identical defect is formed during 30 kV-STEM imaging as shown in figure 6. Here the W adatom and W vacancy are created within one image frame, suggesting that the adatom originates from the vacant position. Also in this case undercoordinated S atoms relax radially outward to form a nanopore. However, now the complete defect structure is not stable as it heals already in the next image frame.

Overall, during the continuous 30 and 60 kV-STEM imaging of 2D WS_2 we have observed the creation of various defects that are invariant to the electron beam energy, including point defects, line defects, trefoil defects, adatom bond rotation defects, nanopores and holes. The distinct difference that we observe between the two accelerating voltages is the increased generation and healing rate of defects when the electron beam energy is halved from 60 keV to 30 keV. This phenomenon emphasizes that more energy is transferred to the monolayer crystal during 30 kV-STEM imaging compared to 60 kV-STEM imaging, which emphasizes our claim that electronic excitation and ionization are the dominant electron–matter mechanism proving energy for

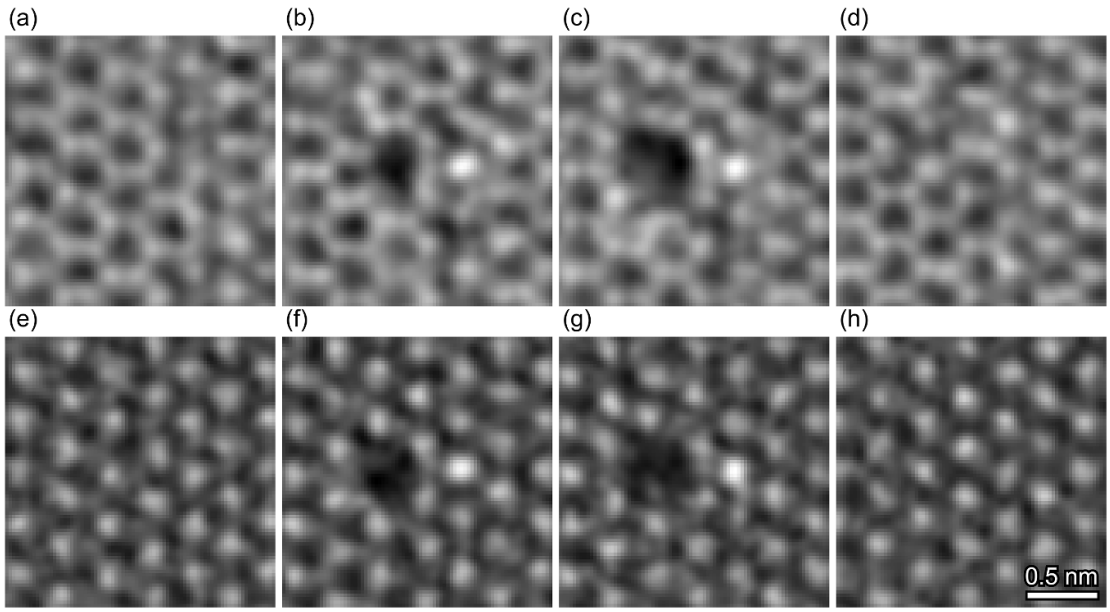

Figure 6. Creation and evolution of a W-adatom induced bond rotational defect and a sub-nanometer pore during 30 kV (a)–(d) iDPC-STEM and (e)–(h) simultaneous ADF-STEM imaging.

defect dynamics and radiation damage during low-voltage STEM analysis.

Relevant parameters for the radiation damage by electronic excitations and ionization are their temporal relaxation rate, spatial delocalization rate and the average time between consecutive electrons during the illumination [15]. In semiconducting 2D materials, typical relaxation times of core holes, valence holes and plasmons are in the range of femtoseconds, picoseconds and nanoseconds, respectively, and delocalize over the lattice within femtoseconds [15, 39]. Even though the electron dose rate (impinging electrons per unit time per unit area) is typically three to four orders of magnitude higher for STEM (due to the focused probe) than for TEM (with parallel illumination), the average time between consecutive electrons is in the range of nanoseconds for STEM (with pA probe current), and in the tens of picoseconds range for TEM (with nA beam current). Therefore, valence excitations in semiconducting 2D materials have sufficient time to relax to the electronic ground state before the next electron arrives during STEM imaging, but not during TEM imaging where valence excitations persist during illumination due to the substantially higher electron arrival rate, and may generate multiple excitations in the end leading to ionization damage. This is also interesting considering that Kretschmer *et al* recently demonstrated with first-principle calculations and 20 kV TEM imaging that (core and) valence electron excitations in 2D MoS_2 can lower the atom's binding energy locally, enabling knock-on sputtering even at ultralow-voltages. Hence, such a multi-electron electronic excitation induced sputtering damage mechanism may be active during TEM imaging, but not in case of STEM. We note, however, that there is no fundamental reason which forbids a single electron to interact with both the electron cloud and the atom nuclei when it impinges on the specimen, in which case there is no difference in radiation damage expected between STEM or TEM in the framework of this mechanism. Nevertheless, this discussion emphasizes how TEM and STEM are principally different and thus may host different radiation damage mechanisms, where STEM has the advantage and possibility to adjust electron delivery to study, minimize and control radiation damage.

Strategies to minimize radiation damage of semiconducting 2D materials like WS_2 with low-voltage STEM should either focus on the reduction of the ionization cross-section by cooling the specimen to cryogenic temperatures [10, 40], or minimization of damage probability by low-dose imaging. The latter requires the use of a dose-efficient imaging technique that maintains atomic resolution and high signal-to-noise-ratio under low-dose (in materials science perspective) conditions. The best available options in this context are sensitive electrostatic potential imaging techniques that optimize the image signal by collecting the majority of transmitted electrons, like iDPC-STEM, iCOM-STEM or electron ptychography [24]. Of these techniques, currently only iDPC-STEM is compatible with fast imaging, and maintains visible signal of both sulfur and tungsten atoms during low-dose imaging down to 5.2×10^3 e Å^{-2} and also 1.7×10^3 e Å^{-2}, although slightly obscured by carbon contamination (figure S4), similar to the demonstration of electron ptychography [24]. In fact, iDPC-STEM has been applied for the ultralow-dose (down

to 40 e $Å^{-2}$) atomic resolution imaging of beam sensitive zeolites [41, 42].

4. Conclusions

In summary, we have quantified radiation damage and investigated beam-induced defect dynamics in semiconducting 2D WS_2 during 30 kV and 60 kV-STEM imaging. Atomic resolution movies are recorded with the fast and direct electrostatic potential imaging technique iDPC-STEM, providing a complete picture and dynamics of all atoms present, not robustly visible in the simultaneously acquired ADF-STEM movies. Based on our quantitative radiation damage analysis, together with the observation of high-energy defect structures, we conclude that electronic excitation and ionization as caused by inelastic scattering are the dominant mechanism leading to defects and damage in semiconducting 2D WS_2 during such low kV-STEM imaging. Accordingly, we observe that defect generation is about a factor two faster at 30 kV than at 60 keV. Moreover, we illuminate the possible advantages of STEM over TEM imaging for the minimization of ionization damage, based on their principally different image forming process and the spatial and temporal characteristics of electronic excitations allowing energy dissipation in between every impinging electron.

Data availability statement

The data that support the findings of this study are available upon reasonable request from the authors.

Acknowledgments

T S Ghiasi, J Peiro, A Kaverzin are thanked for all their time and support in TEM specimen preparation. M Liang is acknowledged for the CVD grown WS_2. Financial support from the Zernike Institute for Advanced Materials and the Groningen Cognitive Systems and Materials Center is gratefully acknowledged.

Conflict of interest

There are no conflict to declare.

ORCID iDs

Sytze de Graaf https://orcid.org/0000-0002-0083-756X
Bart J Kooi https://orcid.org/0000-0002-0311-4105

References

[1] Mak K F and Shan J 2016 Photonics and optoelectronics of 2D semiconductor transition metal dichalcogenides *Nat. Photon.* **10** 216–26
[2] Xia F, Wang H, Xiao D, Dubey M and Ramasubramaniam A 2014 Two-dimensional material nanophotonics *Nat. Photon.* **8** 899
[3] Tombros N, Jozsa C, Popinciuc M, Jonkman H T and van Wees B J 2007 Electronic spin transport and spin precession in single graphene layers at room temperature *Nature* **448** 571–4
[4] Manzeli S, Ovchinnikov D, Pasquier D, Yazyev O V and Kis A 2017 2D transition metal dichalcogenides *Nat. Rev. Mater.* **2** 1–15
[5] Wang S, Robertson A and Warner H J 2018 Atomic structure of defects and dopants in 2D layered transition metal dichalcogenides *Chem. Soc. Rev.* **47** 6764–94
[6] Dyck O, Kim S, Kalinin S V and Jesse S 2017 Placing single atoms in graphene with a scanning transmission electron microscope *Appl. Phys. Lett.* **111** 113104
[7] Susi T, Meyer J C and Kotakoski J 2017 Manipulating low-dimensional materials down to the level of single atoms with electron irradiation *Ultramicroscopy* **180** 163–72
[8] Komsa H-P, Kotakoski J, Kurasch S, Lehtinen O, Kaiser U and Krasheninnikov A V 2012 Two-dimensional transition metal dichalcogenides under electron irradiation: defect production and doping *Phys. Rev. Lett.* **109** 035503
[9] Leuthner G T, Hummel S, Mangler C, Pennycook T J, Susi T, Meyer J C and Kotakoski J 2019 Scanning transmission electron microscopy under controlled low-pressure atmospheres *Ultramicroscopy* **203** 76–81
[10] Egerton R F, Li P and Malac M 2004 Radiation damage in the TEM and SEM *Micron* **35** 399–409
[11] Egerton R F 2012 Mechanisms of radiation damage in beam-sensitive specimens, for TEM accelerating voltages between 10 and 300 KV *Microsc. Res. Tech.* **75** 1550–6
[12] Egerton R F 2019 Radiation damage to organic and inorganic specimens in the TEM *Micron* **119** 72–87
[13] Sawada H, Sasaki T, Hosokawa F and Suenaga K 2015 Atomic-resolution STEM imaging of graphene at low voltage of 30 KV with resolution enhancement by using large convergence angle *Phys. Rev. Lett.* **114** 166102
[14] Kaiser U *et al* 2011 Transmission electron microscopy at 20 kV for imaging and spectroscopy *Ultramicroscopy* **111** 1239–46
[15] Kretschmer S, Lehnert T, Kaiser U and Krasheninnikov A V 2020 Formation of defects in two-dimensional MoS_2 in the transmission electron microscope at electron energies below the knock-on threshold: the role of electronic excitations *Nano Lett.* **20** 2865–70
[16] Sasaki T, Sawada H, Hosokawa F, Sato Y and Suenaga K 2014 Aberration-corrected STEM/TEM imaging at 15 kV *Ultramicroscopy* **145** 50–55
[17] Lazic I, Bosch E G T, Lazar S, Wirix M and Yücelen E 2016 Integrated differential phase contrast (IDPC)–direct phase imaging in STEM for thin samples *Microsc. Microanal.* **22** 36–37
[18] de Graaf S, Ahmadi M, Lazić I, Bosch E G T and Kooi B J 2021 Real-time imaging of atomic potentials in 2D materials with 30 KeV electrons (arXiv:2102.12159 [Cond-mat])
[19] Nukala P *et al* 2021 Reversible oxygen migration and phase transitions in hafnia-based ferroelectric devices *Science* **372** 630–5
[20] Nukala P, Ahmadi M, Antoja-Lleonart J, de Graaf S, Wei Y, Zandbergen H W, Kooi B J and Noheda B 2021 *In situ* heating studies on temperature-induced phase transitions in epitaxial $Hf_{0.5}Zr_{0.5}O_2/La_{0.67}Sr_{0.33}MnO_3$ heterostructures *Appl. Phys. Lett.* **118** 062901
[21] Shen B *et al* 2021 A single-molecule van der Waals compass *Nature* **592** 541–4

[22] de Graaf S, Momand J, Mitterbauer C, Lazar S and Kooi B J 2020 Resolving hydrogen atoms at metal-metal hydride interfaces *Sci. Adv.* **6** eaay4312
[23] Lazić I, Bosch E G T and Lazar S 2016 Phase contrast STEM for thin samples: integrated differential phase contrast *Ultramicroscopy* **160** 265–80
[24] Jiang Y *et al* 2018 Electron ptychography of 2D materials to deep sub-ångström resolution *Nature* **559** 343–9
[25] Schindelin J *et al* 2012 Fiji: an open-source platform for biological-image analysis *Nat. Methods* **9** 676–82
[26] Schindelin J, Rueden C T, Hiner M C and Eliceiri K W 2015 The ImageJ ecosystem: an open platform for biomedical image analysis *Mol. Reprod. Dev.* **82** 518–29
[27] Zhou W, Zou X, Najmaei S, Liu Z, Shi Y, Kong J, Lou J, Ajayan P M, Yakobson B I and Idrobo J-C 2013 Intrinsic structural defects in monolayer molybdenum disulfide *Nano Lett.* **13** 2615–22
[28] Komsa H-P and Krasheninnikov A V 2017 Engineering the electronic properties of two-dimensional transition metal dichalcogenides by introducing mirror twin boundaries *Adv. Electron. Mater.* **3** 1600468
[29] Wang S, Lee G-D, Lee S, Yoon E and Warner J H 2016 Detailed atomic reconstruction of extended line defects in monolayer MoS_2 *ACS Nano* **10** 5419–30
[30] Chen Q, Li H, Zhou S, Xu W, Chen J, Sawada H, Allen C S, Kirkland A I, Grossman J C and Warner J H 2018 Ultralong 1D vacancy channels for rapid atomic migration during 2D void formation in monolayer MoS_2 *ACS Nano* **12** 7721–30
[31] Komsa H-P, Kurasch S, Lehtinen O, Kaiser U and Krasheninnikov A V 2013 From point to extended defects in two-dimensional MoS_2: evolution of atomic structure under electron irradiation *Phys. Rev.* B **88** 035301
[32] Bethe H 1930 Zur theorie des durchgangs schneller korpuskularstrahlen durch materie *Ann. Phys.* **397** 325–400
[33] Inokuti M, Kim Y-K and Platzman R L 1967 Total cross sections for inelastic scattering of charged particles by atoms and molecules. I. A sum rule for the Bethe cross sections and its application to the helium atom *Phys. Rev.* **164** 55–61
[34] Lin Y-C *et al* 2015 Three-fold rotational defects in two-dimensional transition metal dichalcogenides *Nat. Commun.* **6** 6736
[35] Yoshimura A, Lamparski M, Kharche N and Meunier V 2018 First-principles simulation of local response in transition metal dichalcogenides under electron irradiation *Nanoscale* **10** 2388–97
[36] Shin D, Wang G, Han M, Lin Z, O'Hara A, Chen F, Lin J and Pantelides S T 2021 Preferential hole defect formation in monolayer WS_2 by electron-beam irradiation *Phys. Rev. Mater.* **5** 044002
[37] Ryu G H, France-Lanord A, Wen Y, Zhou S, Grossman J C and Warner J H 2018 Atomic structure and dynamics of self-limiting sub-nanometer pores in monolayer WS_2 *ACS Nano* **12** 11638–47
[38] Jiang N 2015 Electron beam damage in oxides: a review *Rep. Prog. Phys.* **79** 016501
[39] Susi T, Meyer J C and Kotakoski J 2019 Quantifying transmission electron microscopy irradiation effects using two-dimensional materials *Nat. Rev. Phys.* **1** 397–405
[40] Egerton R F 2013 Control of radiation damage in the TEM *Ultramicroscopy* **127** 100–8
[41] Liu L, Wang N, Zhu C, Liu X, Zhu Y, Guo P, Alfilfil L, Dong X, Zhang D and Han Y 2020 Direct imaging of atomically dispersed molybdenum that enables location of aluminum in the framework of zeolite ZSM-5 *Angew. Chem., Int. Ed.* **59** 819–25
[42] Shen B, Chen X, Cai D, Xiong H, Liu X, Meng C, Han Y and Wei F 2020 Atomic spatial and temporal imaging of local structures and light elements inside zeolite frameworks *Adv. Mater.* **32** 1906103